Multiscale simulations of copper electrodeposition onto a resistive substrate

T. O. Drews
S. Krishnan
J. C. Alameda, Jr.
D. Gannon
R. D. Braatz
R. C. Alkire

During the initial stages of copper electrodeposition onto a thin seed layer, a nonuniform potential distribution arises, resulting in local variations in growth rate and deposit morphology. Early stages of morphology evolution during copper electrodeposition are of practical importance but have not been well studied. Here, a new multiscale approach is developed for numerical simulation of the effect of a macroscopic potential distribution along a seed layer on microscopic local roughness evolution. The key contribution is a generic method for coupling multiple computer codes, and the demonstration of its use. The macroscopic code passes the local potential at ten points along the seed layer to ten kinetic Monte Carlo codes, each of which simulates additive-free copper electrodeposition and roughness evolution on an initially flat surface. Periodically, each Monte Carlo code computes the local film thickness and passes it back to the resistance code, which updates the potential distribution for the next iteration. Results are obtained for a wide range of parameter space including both constant-potential and constant-current operation. A confirmation procedure was developed to verify that the multiscale approach (using small Monte Carlo simulation domains with periodic boundary conditions) does not significantly alter the physical accuracy of the simulations.

Introduction

Precise control of film uniformity and morphology during the fabrication of electrodeposited on-chip copper interconnections is essential [1]. During the initial stages of electrodeposition, the electrical resistance of the barrier film/seed layer causes potential variations between the center of the wafer and the periphery, where electrical contact is made [2]. Owing to the potential dependence of nucleation, growth, and roughness evolution processes, the deposit morphology can thus vary with radial position and can adversely affect product quality. The development of mathematical models for predicting roughness evolution in the presence of a potential distribution represents an important technological objective; in addition, careful experimental measurements on roughness evolution contain information about growth processes that can be extracted only by mathematical analysis of the data. For interconnect applications, a multiscale modeling approach is required which integrates a macroscopic continuum model (for the potential distribution in the resistive substrate) with multiple microscopic stochastic models (of morphology evolution at various positions along the wafer). Moreover, not only are the length scales widely disparate, but so also are the time scales, which range from fast local stochastic events associated with potential-dependent electrodeposition and surface roughness evolution, to

Contact author: R. C. Alkire at *r-alkire@uiuc.edu*.

©**Copyright** 2005 by International Business Machines Corporation. Copying in printed form for private use is permitted without payment of royalty provided that (1) each reproduction is done without alteration and (2) the *Journal* reference and IBM copyright notice are included on the first page. The title and abstract, but no other portions, of this paper may be copied or distributed royalty free without further permission by computer-based and other information-service systems. Permission to *republish* any other portion of this paper must be obtained from the Editor.

0018-8646/05/$5.00 © 2005 IBM

slow variations that occur at longer time scales as the electrical resistance changes during growth of the metal film. The challenge of simulating coupled dynamic processes that span wide ranges of time and length scales is of broad interest [3]. Multiscale methods are now beginning to emerge that provide a systematic and correct connection between events at different scales. The novel feature of the present work is a generic method for coupling multiple codes so that they interact with one another in a stable manner during the course of a multiscale simulation of distributed behavior.

Several processing approaches have been suggested for ameliorating electrical resistance effects during thin-film electrodeposition. Landau et al. [4] reduced resistance effects during deposition onto thin seed layers by lowering the sulfuric acid concentration, thereby creating a lower-conductivity electrolyte while increasing the copper concentration; this is possible because reducing the sulfuric acid concentration enhances the copper solubility. Takahashi [5] proposed methods of maintaining a more uniform current distribution during initial stages of deposition onto 500-Å-thick Ta barrier films, where the film resistance dominates over solution resistance. He used organic additives that reduce the exchange current density of the deposition reaction and decrease the cupric ion concentration while keeping the sulfuric acid concentration fixed. He also suggested starting the deposition process at a low applied current and then gradually increasing the applied current, keeping the plating rate at the center of the electrode at a certain percentage of the plating rate at the outer edge of the electrode once deposition progressed. These improvements focus on minimizing the "terminal effect," by which the deposit occurs preferentially near the electrical contact point because of significant electrical resistance in the electrode.

Mathematical models of electrodeposition onto resistive substrates have been carried out to date with continuum models that simulate macroscopic phenomena associated with the potential distribution and reaction rate variation across the wafer [6], as well as convective mass transfer and the effect of deposit thickness evolution [7]. More recently, Matlosz et al. [8] simulated electrodeposition onto resistive substrates; their model included deposit growth and varying substrate conductance that resulted from the growth. Lanzi and Landau [9] simulated the terminal effect for general geometry cells and estimated the magnitude of the current nonuniformity that results from the terminal effect in systems where Tafel kinetics are present. Kawamoto [10] computed the secondary current distribution for 2D cells with a resistive electrode without considering transient deposit growth. Deligianni et al. [11] simulated a cup plater with a continuous peripheral contact and passive elements that helped shape the potential field to give an almost uniform current distribution. They accounted for film growth in the model by changing the sheet conductance over time, but kept the seed layer thickness constant. While such continuum models can address the issue of the nonuniform potential distribution, they have a blind spot that blocks them from addressing small-scale stochastic events such as nucleation, growth, surface roughening, and morphology evolution during the early stages of electrodeposition.

The objective of the present work is to simulate behavior over the entire wafer while also predicting local morphology evolution. A novel multiscale simulation approach is described that utilizes a generic method for linking multiple computer codes. The macroscopic code passes the local potential at ten points along the seed layer to ten kinetic Monte Carlo codes, each of which simulates additive-free copper electrodeposition and roughness evolution on an initially flat surface. Periodically, each Monte Carlo code computes the local film thickness and passes it back to the resistance code which updates the potential distribution for the next iteration. Speed-up arises in large part because the Monte Carlo codes do not simulate the entire radius of the wafer, nor do they pass information to one another. The validity of this approach is analyzed with a confirmation procedure. Simulation results are presented for both constant potential (because scientific experiments on nucleation and growth are usually carried out at constant potential) and constant current (which is typically used for industrial plating operations). The method provides a "reusable" multiscale simulation approach that has the potential for contributions well beyond the specific application demonstrated here.

Model descriptions

This section contains a description of the macroscopic resistance model, the microscopic Monte Carlo model, and the code linkage by which they were coupled to form the multiscale model.

Resistance model

The resistance model is based on several assumptions: 1) The counter electrode is configured so that the primary current distribution would be uniform in the absence of electrode resistance effects. 2) The electrical double layer and the mass transfer diffusion boundary layer attain a steady state rapidly compared with the slow transient process of deposit thickening. 3) A substantial number of electrical contact points are made around the edge of the wafer so that azimuthal potential variations are negligible. 4) Only one copper electrodeposition reaction occurs, and there are no additives in the deposition bath. 5) From a macroscopic viewpoint, the surface of the

working electrode remains smooth during the course of deposition; surface roughness is treated solely in the Monte Carlo simulations. 6) The ohmic resistance in the solution is negligible with respect to other resistances in the cell. 7) The electrolyte contains an excess of supporting electrolyte so that migration of copper ions in the solution is negligible. 8) The solution is stirred such that the cupric ions are uniformly accessible to the surface at all points. Many of these simplifying assumptions can readily be modified in order to deal with more complex situations. Lists of the symbols used may be found in appendices at the end of the paper.

The general approach used for the model follows the procedures outlined in detail previously [7]. Resistance to the passage of electrons through the seed/barrier layer obeys Ohm's law,

$$i(r,t) = -\sigma \frac{d\phi_m(r,t)}{dr}. \quad (1)$$

The electronic current in the metal phase, $i(r, t)$, varies in the radial direction depending on the cross-sectional area and the reaction rate distribution,

$$\frac{d[H(r,t)i(r,t)r]}{dr} = -j(r,t)r. \quad (2)$$

The electrodeposition reaction rate, $j(r, t)$, also varies with radial position across the wafer; it is described by the Butler–Volmer equation, which includes the local surface concentration at the electrode,

$$j(r,t) = i_0\left[e^{\frac{\alpha_T nF\eta(r,t)}{RT}} - \left(\frac{c_s(r,t)}{c_b}\right)e^{\frac{(\alpha_T-1)nF\eta(r,t)}{RT}}\right]. \quad (3)$$

The overpotential in Equation (3), $\eta(r, t)$, is the sum of the charge-transfer overpotential and the concentration overpotential and is defined as

$$\eta(r,t) = [\phi_m(r,t) - \phi_s^\bullet] - [\phi_m^e - \phi_s^e]. \quad (4)$$

The applied potential is related to the various overpotentials by the expression

$$\begin{aligned}[(\phi_m^\bullet - \phi_s^\bullet) - (\phi_m^e - \phi_s^e)] = {} & [\phi_m^\bullet - \phi_m(r,t)] \\ & + [\phi_s^s(r,t) - \phi_s^\bullet] \\ & + [\phi_m(r,t) - \phi_s^s(r,t)] \\ & - [\phi_m^e - \phi_s^e], \end{aligned} \quad (5)$$

where the ohmic overpotential is

$$\eta_\Omega = [\phi_m^\bullet - \phi_m(r,t)], \quad (6)$$

the concentration overpotential is

$$\eta_c = [\phi_s^s(r,t) - \phi_s^\bullet], \quad (7)$$

and the charge-transfer overpotential is

$$\eta_s = [\phi_m(r,t) - \phi_s^s(r,t)] - [\phi_m^e - \phi_s^e]. \quad (8)$$

The concentration overpotential is related to the concentration difference across the diffusion boundary layer by

$$\phi_s^s(r,t) - \phi_s^\bullet = \left(\frac{RT}{nF}\right)\ln\left(\frac{c_s(r,t)}{c_b}\right). \quad (9)$$

The local deposition rate, $j(r, t)$, can also be obtained from the concentration difference across the diffusion layer in conjunction with the mass-transfer coefficient,

$$j(r,t) = -nFk[c_b - c_s(r,t)]. \quad (10)$$

The following dimensionless parameters are used to rewrite the equations in dimensionless form:

$$\xi = \frac{R_0^2 nFi_0}{RT\sigma H_0},$$

$$A(r,t) = \frac{H(r,t)}{H_0(r,t)},$$

$$\Gamma = \frac{n^2F^2kc_bR_0^2}{RT\sigma H_0},$$

$$R_a = \frac{r}{R_0},$$

$$\beta_{CD}(\tau) = \frac{H^\bullet R_0 i^\bullet nF}{RT\sigma H_0},$$

$$C_s(r,t) = \frac{c_s(r,t)}{c_b} = \frac{1 + \frac{\xi}{\Gamma}e^{\alpha_T(\Phi_m+\Phi_a)}}{1 + \frac{\xi}{\Gamma}e^{(\alpha_T-1)(\Phi_m+\Phi_a)}},$$

$$\Phi_a = \left(\frac{nF}{RT}\right)[(\phi_m^\bullet - \phi_s^\bullet) - (\phi_m^e - \phi_s^e)],$$

and

$$\Phi_m = \left(\frac{nF}{RT}\right)[\phi_m(r,t) - \phi_m^\bullet].$$

The parameter ξ represents the ratio of ohmic resistance to charge-transfer resistance. The parameter Γ is the ratio of ohmic resistance to mass-transfer resistance.

Equations (1)–(10) can be combined in dimensionless form to give

$$(R_aA\Phi_m')' = \xi R_a\left[e^{\alpha_T(\Phi_m+\Phi_a)} - \left(\frac{1 + \frac{\xi}{\Gamma}e^{\alpha_T(\Phi_m+\Phi_a)}}{1 + \frac{\xi}{\Gamma}e^{(\alpha_T-1)(\Phi_m+\Phi_a)}}\right)e^{(\alpha_T-1)(\Phi_m+\Phi_a)}\right], \quad (11)$$

where the prime refers to differentiation with respect to R_a. Equation (11) was solved repeatedly during the course of a deposition simulation which, in this work, lasted 120 s. The time step between macroscopic simulations was 0.005 s, so that 24,000 simulations were carried out. At each time step, the deposit thickness distribution, $A(r, t)$, was provided by the Monte Carlo code.

Constant potential

Constant-potential simulations are performed by solving Equation (11) with the boundary conditions

$$\Phi'_m(0,\tau) = 0 \tag{12}$$

and

$$\Phi_m(1,\tau) = 0. \tag{13}$$

Equation (12) is a symmetry boundary condition that describes the potential gradient in the electrode at the center of the wafer. Equation (13) is the boundary condition at the electrical contact point at the edge of the wafer.

The dimensionless current distribution can then be computed as

$$J(R_a,\tau) = \left(\frac{\xi}{\beta_{CD}}\right)[e^{\alpha_T(\Phi_m+\Phi_a)} - C_s e^{(\alpha_T-1)(\Phi_m+\Phi_a)}]. \tag{14}$$

The foregoing equations and dimensionless variables completely describe the resistance model when a constant potential is applied. In the coupled simulations described below, deposit thickness information is obtained from the Monte Carlo simulation codes. (If the resistance code were not coupled to the Monte Carlo code, the deposit thickness would be computed from Faraday's law.) The overpotential in the electrode that is passed to the Monte Carlo model is

$$\eta = \phi_a + [\phi_m(r,t) - \phi_m^\bullet]. \tag{15}$$

A linear equation solver that uses LU (lower–upper) decomposition with back substitution [12] was used to solve Equation (11) with boundary conditions (12) and (13). The equation was linearized about a trial solution and placed in finite difference form. When the code was run standalone for one iteration with 50 equally spaced nodes, the simulation took less than one second to complete on a Silicon Graphics SGI** Origin** 2000.

Constant current

Constant-current boundary conditions were used for a process operating at 15 mA/cm^2 which, on a 300-mm-diameter wafer (707 cm^2), would support 10.6 A. The current density was the nominal value based on the projected area of a planar wafer; i.e., no account was taken of any additional surface area created by features. The current entering the peripheral contacts to the wafer seed layer thus remained constant at 10.6 A during the course of the simulation. The boundary condition for constant-current operation is

$$\Phi'_m(1,\tau) = -\frac{\Xi}{2\pi}, \tag{16}$$

where $\Xi = [nFI/RT\sigma H(r,t)]$ represents the ratio of ohmic resistance to charge-transfer resistance. Equations (10), (12), (13), and (16) were solved with a nonlinear equation solver [12] that used a globally convergent Newton–Raphson method.

Monte Carlo code

Stochastic simulations of electrochemical deposition of copper onto an initially flat, featureless copper surface were carried out with a kinetic Monte Carlo (KMC) code. The procedures used were very similar to those reported in detail elsewhere [13], and are briefly summarized here. The simulation space for the Monte Carlo code [14, 15] consisted of a cubic lattice which was sized at the mesoscale [16] and whose blocks or "pseudoparticles" represented clusters of molecules of a given species in the deposition bath [17–20]. Blocks were assumed to be homogeneous in both phase and composition. The typical block size used for simulations in this study was 100 nm. In such a block, there would be approximately 8.5×10^7 Cu^{2+} ions for the concentration used in this work. The size of the Monte Carlo domain used was 50 blocks wide, 50 blocks high, and 50 blocks deep. While it is clear that smaller block sizes would be required for detailed applications, the effort in the present work was directed toward developing the computational methodology. In other recent work using more efficient Monte Carlo methods, for example, we have reported on the use of 0.5-nm blocks for trench-infill simulations [21], as well as atomic-scale pseudoparticles for nucleation simulations [22].

Following the general approach described in Reference [13], the Monte Carlo domain had periodic boundary conditions in the x and y directions, an impenetrable boundary at the electrode surface (in the z direction), and a link to a small-scale 1D continuum code at the top boundary in the z direction. At the electrode surface, the reaction mechanism followed a two-step process. First, Cu^{2+} ions arriving at the surface by bulk diffusion react by a one-electron transfer and adsorption of Cu^+ onto the surface:

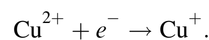

$$Cu^{2+} + e^- \rightarrow Cu^+.$$

The cuprous adions move by surface diffusion to a second location, where they react via a second one-electrode transfer and become incorporated into the crystal lattice:

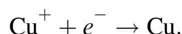

$Cu^{+} + e^{-} \rightarrow Cu.$

The value of overpotential used for the electrochemical reactions was obtained from the macroscopic resistance code. The top boundary of the Monte Carlo domain was linked to a small-scale 1D finite difference code that provided diffusion fluxes of Cu^{2+} into the Monte Carlo domain; the Monte Carlo code provided the concentration of Cu^{2+} to the small-scale continuum code. The small-scale continuum code domain was 50 μm thick, which corresponded to the same value of mass-transfer coefficient as was used in the macroscopic resistance code. Concentrations used internally by the Monte Carlo code were not shared with the macroscopic resistance code; in more recent work, we have developed improved Monte Carlo algorithms that eliminate altogether the need to handle bulk diffusion phenomena in the stochastic code.

The time step used for KMC simulations was selected as the inverse of the largest frequency in the system, so that the "full dynamics" of the system would be captured (2.8×10^{-6} s for the system at hand [13]). At a given Monte Carlo time step, a pseudoparticle can make a maximum of only one move. The possible moves include bulk diffusion, reaction/adsorption, and surface diffusion. The moves made by a pseudoparticle are a function of the location of the particle in the simulation space and the number and type of nearest neighbors. For each macroscopic time step (0.005 s), there were 1.8×10^{3} Monte Carlo time steps.

Upon completion of the each time step in the resistance code, the surface roughness was stored. At the completion of the entire computation, the surface roughness evolution data were evaluated by the well-established method of scaling analysis of the interface width [23]. According to that approach, the root-mean-squared height of the roughness of self-affine surfaces scales as

$$h(L, t) = L^{\alpha} f\left(\frac{t}{L^{\alpha/\beta}}\right), \qquad (17)$$

where the two exponents, α and β, respectively characterize the spatial and temporal evolution of the surface roughness. The function $f(t/L^{\alpha/\beta})$ behaves as $(t/L^{\alpha/\beta})^{\beta}$ for $(t/L^{\alpha/\beta}) \ll 1$, for which $h \propto t^{\beta}$, and $f(t/L^{\alpha/\beta})$ approaches a constant for $(t/L^{\alpha/\beta}) \gg 1$, for which $h \propto L^{\alpha}$ [23]. Therefore, the spatial scaling exponent α may be found by computing the slope of the initial points in a plot of the surface roughness as a function of distance across the surface. The temporal scaling exponent β is determined by computing the slope of a log plot of saturation roughness, which is the limit of the roughness over large distances across the surface, as a function of time.

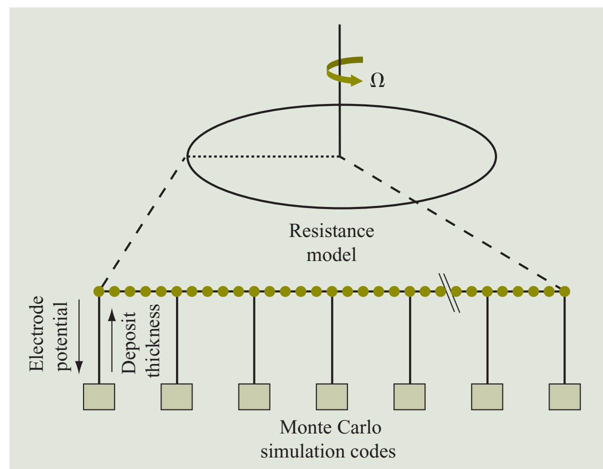

Figure 1

Diagram of the code linkage and information passed between the resistance model and the Monte Carlo simulation codes.

Code linkage

The resistance model was linked to multiple Monte Carlo simulation codes to perform coupled simulations, as shown in **Figure 1.** The coupled simulation follows a standard "master–worker" computational paradigm, where the resistance model is the master code and the Monte Carlo simulations are the workers. The following example sequence begins after the resistance model runs for one time step to obtain a pseudo-steady-state solution for the potential distribution in the electrode by solving Equation (11). Since the resistance model is linked to ten Monte Carlo codes, the local overpotential, Equation (15), is averaged over five-node segments and passed to the ten Monte Carlo simulation codes. Each Monte Carlo simulation code then runs for a pre-set amount of time (0.005 s), after which it computes the average deposit thickness across the surface and passes that value back to the resistance model. Since there are fewer Monte Carlo simulations than there are nodes in the resistance code, the resistance model uses a spline-fitting routine [12] for the deposit thickness to estimate a value of the deposit thickness at each node of the continuum code. After all of the Monte Carlo simulation codes have passed their average deposit thickness to the resistance model, the resistance model runs again. This sequence is repeated (24,000 times for the results given here) until the specified amount of deposition time (120 s for the results given here) has been completed. A 120-s simulation typically required three to four days to complete. It was found that almost all of the time required for the coupled simulations was consumed by the Monte Carlo simulations.

The application manager that controls the workflow sequencing operations and exchange of information

Table 1 Set of base case physical parameters and dimensionless parameters used in the coupled simulations.

Resistance code physical parameters

Symbol	*Parameter*	*Value*
α_T	Tafel slope	0.5
ρ_{Cu}	Density of copper	8.96 (mole/cm^3)
M	Molecular weight of Cu	63.546 (g/g-mole)
σ	Electrode conductivity	5×10^5 (1/Ω-cm)
R	Ideal gas constant	8.31 (J/g-mole-K)
T	Temperature	294 (K)
n	Cu charge equivalents	2 (eq/mole)
R_0	Electrode radius	15 (cm)
F	Faraday's constant	96,500 (C/eq)
i_0	Exchange current density	1×10^{-3} (A/cm^2)
H_0	Initial deposit thickness	1×10^{-5} (cm)
k	Mass-transfer coefficient	1.2×10^{-3} (cm/s)
c_b	Cu^{2+} bulk concentration	5×10^{-4} (mole/cm^3)
Φ_a	Dimensionless applied potential	−10
I	Applied current	10.6 A

Resistance code dimensionless variables

Operating conditions	ξ	Γ	β_{DT}
$\Phi_a = -10$, $H_0 = 1 \times 10^{-5}$ (cm)	3.55	411.65	30.26
$\Phi_a = -10$, $H_0 = 5 \times 10^{-6}$ (cm)	7.11	823.30	43.31
$\Phi_a = -10$, $H_0 = 1 \times 10^{-6}$ (cm)	35.55	4,116.52	91.19
$I = 10.6$, $H_0 = 1 \times 10^{-5}$ (cm)	3.55	411.65	26.65
$I = 10.6$, $H_0 = 5 \times 10^{-6}$ (cm)	7.11	823.30	53.31
$I = 10.6$, $H_0 = 1 \times 10^{-6}$ (cm)	35.55	4,116.52	266.54

Monte Carlo code physical parameters

Parameter	*Value*
Cu^{2+} bulk diffusion rate	6.0×10^8 (nm^2/s)
Cu^{2+} adsorption rate	150 (nm/s)
Cu^{2+} adsorption Tafel slope	0.339
Cu^+ surface diffusion rate	2.0×10^8 (nm^2/s)
Cu^+ step energy barrier	-1.5×10^{-20} (J)
Cu^+ broken face energy barrier	-5.0×10^{-22} (J)
Cu^+ new face energy barrier	5.0×10^{-22} (J)
Cu^+ incorporation rate	2.0×10^4 (nm^2/s)
Cu^+ incorporation transfer coefficient	−0.4
Cu^+ incorporation transfer coefficient contribution from Cu	0.2

between the individual models is similar to those reported in previous work [14]. The application manager is generic in the sense that users can change the codes that are linked together as well as the number of codes that are linked together, such as the number of Monte Carlo simulations linked to the resistance model. The models are linked via direct port connections. Information is passed between the models in files. The following example

illustrates how the linkage is performed, beginning when the resistance model has completed one time step. The resistance model writes multiple files, each with a different overpotential, which triggers the resistance model application manager to alert the Monte Carlo application manager of the existence of the files. The Monte Carlo simulation codes then read and continue the simulations with the new overpotentials. When each Monte Carlo simulation code completes its time step, the code writes a file that contains the average deposit height in the Monte Carlo domain, which is passed to the resistance model. When all Monte Carlo codes have written their files, the resistance model application manager runs the resistance model, and a new sequence begins. These iterations continue until a user-specified amount of deposition time is reached.

Simulations were performed on an SGI R10000** machine and an SGI Power Challenge** with ten R8000** CPUs located at Indiana University. A 120-s coupled simulation required three to four days to complete on these machines. Simulations were also performed at the National Center for Supercomputing Applications (NCSA) at the University of Illinois with use of an SGI Origin 2000, and required comparable time to complete. The distributed system used to demonstrate the linkage for an electrodeposition application is but one of many such continuum/stochastic multiscale systems that could be investigated with the general approach described here.

Results and discussion

To demonstrate the multiscale modeling approach, simulations were carried out assuming constant applied potential and constant applied current. The set of base case parameters used in all of the simulations, along with the values of key dimensionless parameters, are listed in **Table 1.** The set of operating conditions included three simulations run with different seed layer thicknesses (100 Å, 500 Å, and 1,000 Å) for both constant-potential and constant-current conditions. One simulation was performed with a different initialization of the random number generator in the Monte Carlo simulation codes to determine the variation in the outputs in both the continuum and Monte Carlo codes as a function of the initial state of the random number generator. Finally, a confirmation procedure was implemented to show that the use of small Monte Carlo simulations with a single applied potential and periodic boundary conditions to represent deposition on a larger surface does not lead to physical inaccuracies.

Constant-potential simulations

The initial potential distribution in the wafer for all three seed layer thicknesses with a dimensionless applied potential of –10 is shown in **Figure 2.** As the seed layer thickness decreases, the electrical resistance in the seed layer increases. For the seed layer thickness of 100 Å, the potential in the metal at the center of the wafer ($R_a = 0$) is nearly equal in magnitude to the applied potential. Under such conditions, most of the applied potential is consumed by ohmic effects, with the result that the local deposition rate is very low.

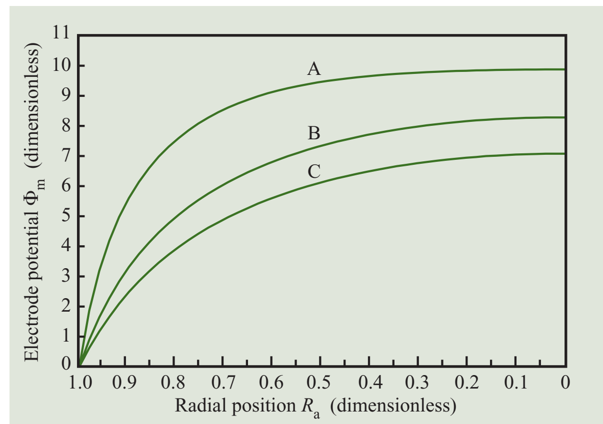

Figure 2

Initial potential distribution in the wafer for seed layer thicknesses of 100 Å, where $\beta_{CD} = 91.19$ (Curve A), 500 Å, where $\beta_{CD} = 43.31$ (Curve B), and 1,000 Å, where $\beta_{CD} = 30.26$ (Curve C), at a constant applied potential of $\Phi_a = -10$ (dimensionless) and using base case physical parameters.

In **Figure 3(a)**, the dimensionless deposit thickness profile is shown for all seed layer thicknesses after 120 s of deposition. The values of the dimensionless deposit thickness are much larger as the seed layer thickness decreases because of the manner in which the deposit thickness is nondimensionalized. In all of the simulations, the deposit thickness at the contact end is two to three times thicker than it is at the center of the wafer. The fact that this phenomenon occurs in the same manner independently of the thickness of the initial seed layer indicates that the temporal evolution of the potential distribution in the wafer occurs in a similar manner for all seed layer thicknesses. If the potential distribution did not evolve in a similar manner, it would leave a footprint in the thickness profile because the deposit would grow differently.

The distribution of the spatial scaling exponent α after 120 s of deposition for all constant-potential simulations is shown in **Figure 3(b)**. The simulations closest to the electrical contact point ($R_a = 1$) tend to have higher values of α, implying that the surface is rougher near the electrical contact end. Considering microscopic events treated by the Monte Carlo code, the higher charge-transfer overpotential at the contact side would result in

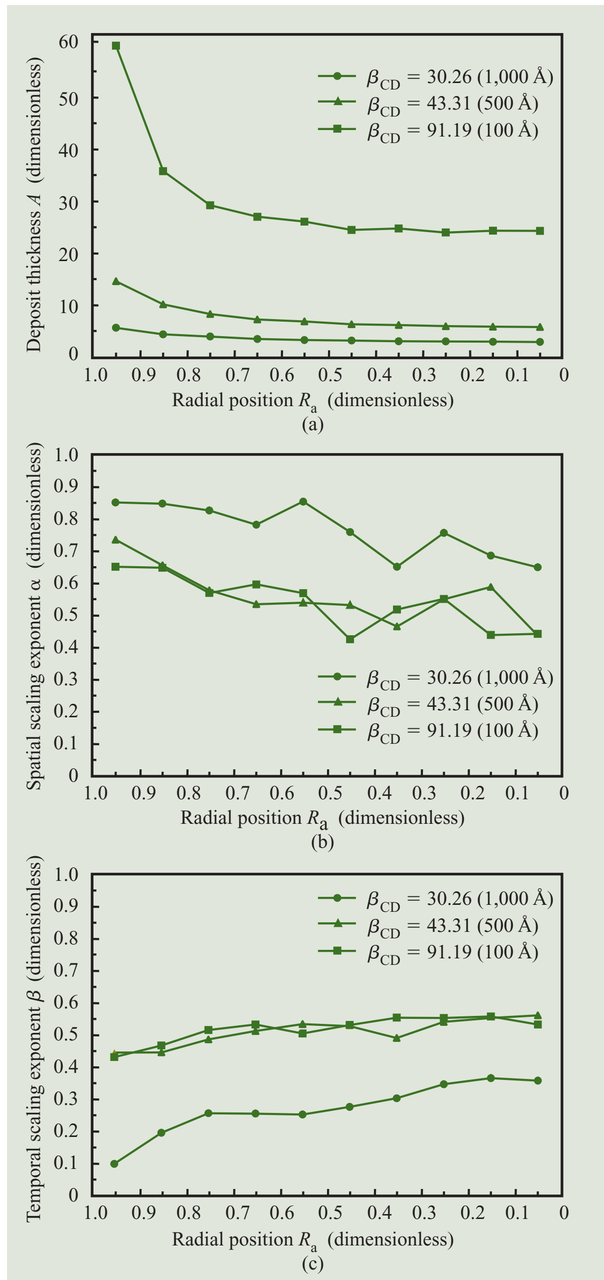

Figure 3

After 120 s of deposition for seed layer thicknesses of 100 Å (β_{CD} = 91.19), 500 Å (β_{CD} = 43.31), and 1,000 Å (β_{CD} = 30.26), at a constant applied potential of $\Phi_a = -10$ and using base case physical parameters: (a) deposit thickness profile; (b) spatial scaling exponent distribution; (c) temporal scaling exponent distribution.

cuprous pseudoparticle ions having less time to move by diffusion along the surface to find low-energy sites to incorporate into the metal. It is also seen in Figure 3(b) that the average value of α decreases everywhere along the

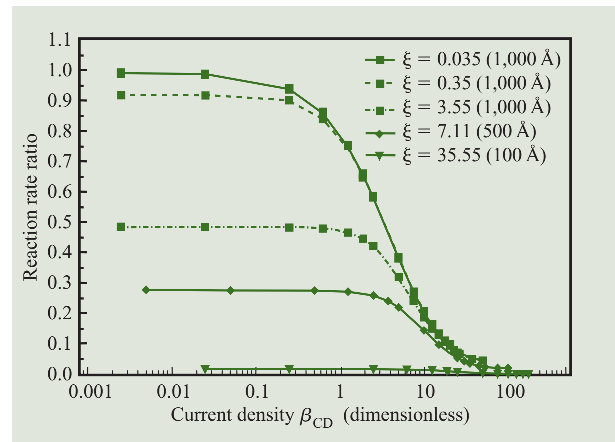

Figure 4

Reaction rate ratio vs. current density at different values of the parameter ξ. The reaction rate ratio is the ratio of the reaction rate at the center of the wafer to the reaction rate at the electrical contact point.

wafer as the seed layer thickness decreases owing to the higher ohmic resistance (thus lower charge-transfer overpotential) associated with thinner seed layers. Moreover, the value of α at the electrical contact point decreases as seed layer thickness decreases; although the value of α at the electrical contact point would be expected to remain constant because the applied potential remains constant, the fact that five nodes in the continuum code are averaged together to compute the potential in the electrode that is passed to the Monte Carlo code causes average potentials at the contact to be not identical for all seed layer thicknesses.

The distribution of the temporal scaling exponent β after 120 s of deposition is shown in **Figure 3(c)** for all seed layers. The values of β for a given position across the wafer decrease as the seed layer thickness increases. The observed variation in β is attributed to the fact that from the beginning to the end of the simulation, the potential in the metal changes more at the center of the wafer than at the electrical contact point.

Constant-current simulations

Simulations performed with only the resistive code are depicted in **Figure 4** in order to show the effect of macroscopic parameters on the current distribution. The ordinate gives the ratio of the reaction rate at the center of the wafer to the reaction rate at the electrical contact point (a value of 1 corresponds to a uniform current distribution). The 1,000-Å (ξ = 3.55), 500-Å (ξ = 7.11), and 100-Å (ξ = 35.55) simulations show that the current distribution is not uniform, even at low current densities, since the reaction rate ratio is less than 1. Decreasing the

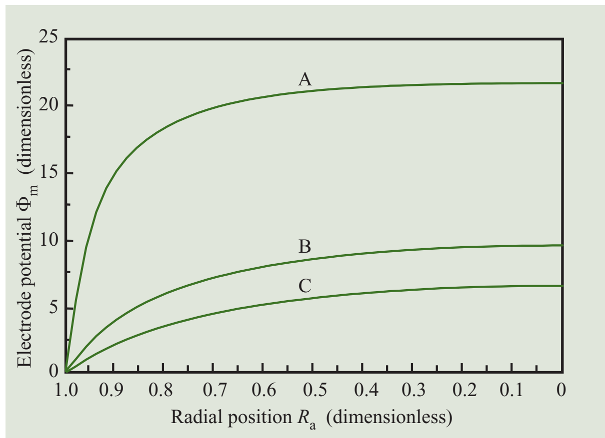

Figure 5

Initial potential distribution at seed layer thicknesses of 100 Å, where $\beta_{CD} = 266.54$ (Curve A), 500 Å, where $\beta_{CD} = 53.31$ (Curve B), and 1,000 Å, where $\beta_{CD} = 26.65$ (Curve C), at a constant applied current of $I = 10.6$ A and using base case physical parameters.

exchange current density by one order of magnitude (to $\xi = 0.35$) for a 1,000-Å-thick seed layer failed to provide a uniform current distribution, although decreasing it by two orders of magnitude (to $\xi = 0.035$) provided a nearly uniform current distribution for low applied currents.

When a constant current is applied, the initial potential distribution in the seed layer depends on its thickness, as seen in **Figure 5.** The variation in the potential distribution as a function of the seed layer thickness is greater for the constant-current results presented in Figure 5 than for the constant-potential conditions presented in Figure 2 because the potential required to satisfy the current demand for the constant-current simulations changes as a function of the seed layer thickness. Moreover, the potential required to meet the current for the 100-Å-thick seed layer is twice as large as the potential applied in the example constant-potential simulations.

The resistive code alone was used to provide the results illustrated in **Figure 6(a)** for the dimensionless deposit thickness profile for all three seed layer thicknesses after 120 s of deposition. The same trends are observed here as in the constant-potential simulations associated with Figure 3(a); in all of the simulations, the deposit thickness at the contact end is two to three times thicker than it is at the center of the wafer. The fact that the deposit thickness at the contact end is two to three times thicker than it is at the center of the wafer regardless of the initial seed layer thickness indicates that the temporal evolution of the potential distribution in the wafer occurs in a similar manner for all seed layer thicknesses.

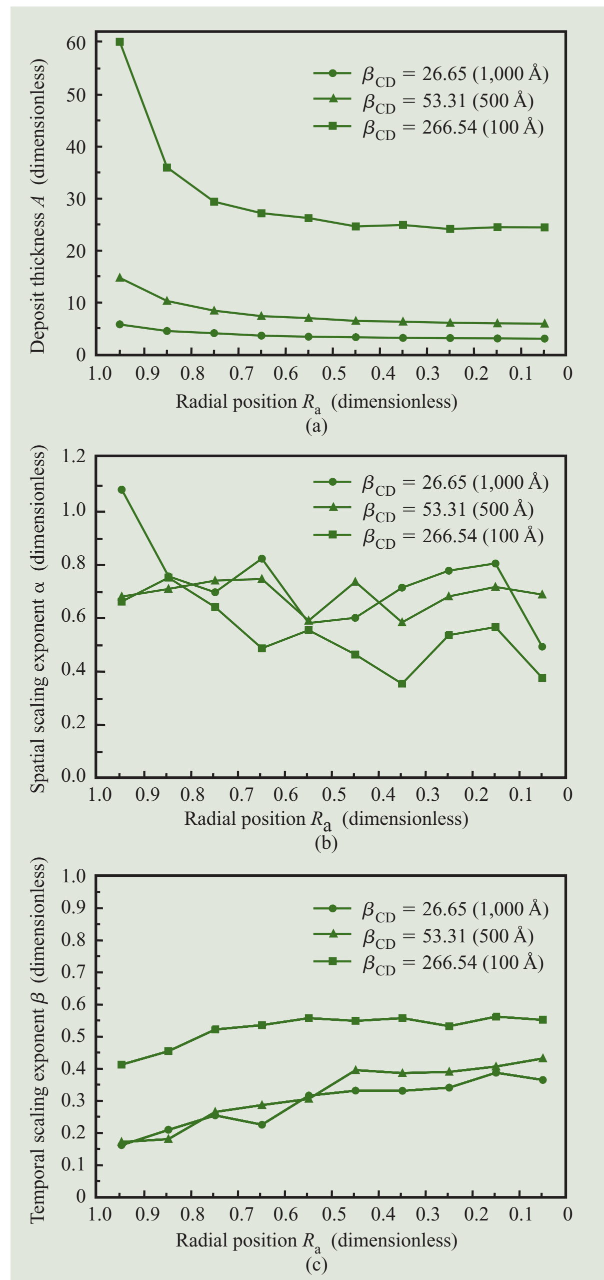

Figure 6

After 120 s of deposition for seed layer thicknesses of 100 Å ($\beta_{CD} = 266.54$), 500 Å ($\beta_{CD} = 53.31$), and 1,000 Å ($\beta_{CD} = 26.65$), at a constant applied current of $I = 10.6$ A and using base case physical parameters: (a) deposit thickness profile; (b) spatial scaling exponent distribution; (c) temporal scaling exponent distribution.

Distributions for the spatial scaling exponent α for all seed layer thicknesses after 120 s of deposition are shown in **Figure 6(b).** The simulations closest to the electrical contact point have the highest values of α, indicating that the surface is roughest there. Additionally, on average,

the values of α decrease as the seed layer thickness decreases. Lower values of α imply that the surface is less rough because the root-mean-squared roughness is not increasing rapidly over short length scales. Figure 5 shows that the potential in the metal decreases as the initial seed layer thickness is decreased, indicating that the current is lower across the wafer for thinner seed layers. If the current were lower, it is expected in the simulations that the surface roughness would be lower because cuprous pseudoparticles would have more time to move by surface diffusion to low-energy sites on the surface and incorporate into the metal.

The distribution of the temporal scaling exponent β after 120 s of deposition is shown in **Figure 6(c)** for all seed layers. The values of β across the wafer decrease as the seed layer thickness decreases. The observed variation in β is attributed to the fact that the potential in the metal changes more at the center of the wafer than at the electrical contact point from the beginning to the end of the simulation. The trends observed for the constant-current simulations are similar to those observed for the constant-potential simulations.

Simulation with different random seed numbers

Since it is a stochastic method, KMC simulations produce results with fluctuations that are dependent on the seed number used in the random number generator. Therefore, one of the test simulations was repeated with a different seed number in the random number generator in all of the Monte Carlo simulation codes to determine the influence of the seed number on the outputs of both the Monte Carlo model and the resistance model. The simulation selected for evaluation was a constant-potential simulation with a dimensionless applied potential of –10 and a 1,000-Å-thick seed layer. The effects of the random seed number are expected to be similar for other operating conditions.

The initial potential distributions for the two simulations are identical because they are not a function of anything generated in the Monte Carlo code and are of a purely continuum nature. The final potential distributions are expected to be different for each simulation, however, since they depend on stochastic results from the Monte Carlo code (i.e., the thickness distribution as a function of time). For the test comparison, it was found that the maximum potential difference, which occurred near the center of the wafer, was less than 10 mV or 0.8 dimensionless potential units, which is 8% of the applied potential.

The ratio of the dimensionless deposit thickness at the contact end to the dimensionless deposit thickness at the center of the wafer was about 2 for both simulations [see Figure 3(a)]. However, the deposit thickness profiles for the two simulations differed by about 25%. Because of the exponential relation between potential and current shown in Equation (3), we note that an 8% difference in potential corresponds roughly to a 25% difference in current density for the conditions at hand. The distributions of the spatial scaling exponent α as well as those for the temporal scaling exponent β were found to be sensitive to the random seed number. The trend that the spatial scaling exponent is larger at the contact end than at the center of the wafer was observed in both simulations; however, the values of the exponent vary by almost 25% at the contact end [the variation at the center of the wafer was lower, as noted in Figure 3(b)]. While the overall trends that the temporal scaling exponent was smaller at the contact end and increased across the wafer were observed in both simulations, the value of the two exponents was found to differ by about 75% at the contact end [the variation at the center of the wafer was lower, as noted in Figure 6(b)].

The influence of the seed number on potential, current, and scaling results points to the need for making a sufficient number of duplicate simulations with random seed numbers in order to average out stochastic noise. Although the coarse-grained stochastic results reported in this study provide approximate representations of behavior, the use of high-throughput computing methods is recommended for obtaining accurate and statistically significant results.

Confirmation procedure

Each Monte Carlo simulation code has periodic boundary conditions in the x and y directions, which means that none of the Monte Carlo simulation codes pass pseudoparticles to one another. In a real system it is in principle possible that copper ions in the solution could move laterally across the wafer to regions where the potential is different, which might affect the scaling analysis results. The following confirmation procedure was therefore carried out to assess whether the scaling analysis results computed by the Monte Carlo simulations are affected by the use of small simulation domains with periodic boundary conditions. The procedure for testing the approximation was to use a single Monte Carlo domain that was twice as wide as the original domains, and then apply the potentials (which change over time) determined from the coupled simulations at two adjacent nodes to separate halves of the Monte Carlo domain. The potentials from two adjacent nodes were averaged together, and the entire simulation was performed with a single set of potentials. Then scaling analysis was performed on each half of the Monte Carlo domain.

The confirmation simulation used the average of the potentials that were supplied to the two Monte Carlo simulation codes which were closest to the electrical

Table 2 Spatial scaling exponent α after 30, 60, 90, and 120 s of deposition for seed layer thickness of 1,000 Å at a constant applied potential of $\Phi_a = -10$ and using base case physical parameters. The confirmation simulation was split in half and the scaling exponents were computed for each half.

Time (s)	*Confirmation simulation* α_c^a (from the electrical contact point to 1.5 cm from the electrical contact point)	*Confirmation simulation* α_c^b (from 1.5 cm to 3.0 cm from the electrical contact point)	*Monte Carlo simulation* α^a (from the electrical contact point to 1.5 cm from the electrical contact point)	*Monte Carlo simulation* α^b (from 1.5 cm to 3.0 cm from the electrical contact point)
30	0.828	1.014	0.984	1.027
60	0.790	0.916	0.938	0.660
90	0.831	0.846	1.004	0.793
120	0.773	0.704	0.852	0.848

Table 3 Temporal scaling exponent β after 120 s of deposition for seed layer thickness of 1,000 Å at a constant applied potential of $\Phi_a = -10$ and using base case physical parameters. The confirmation simulation was split in half and the scaling exponents were computed for each half.

Time (s)	*Confirmation simulation* β_c^a (from the electrical contact point to 1.5 cm from the electrical contact point)	*Confirmation simulation* β_c^b (from 1.5 cm to 3.0 cm from the electrical contact point)	*Monte Carlo simulation* β^a (from the electrical contact point to 1.5 cm from the electrical contact point)	*Monte Carlo simulation* β^b (from 1.5 cm to 3.0 cm from the electrical contact point)
120	0.181	0.198	0.100	0.197

contact point for a dimensionless potential of −10 and a seed layer thickness of 1,000 Å. The results of the confirmation simulation and the two standalone simulations are summarized in **Tables 2** and **3.** In Table 2, the values of the spatial scaling exponent α for four different times are presented. The confirmation domain was split into two identical domains so that scaling analysis could be performed on each part. The values of α for each side of the domain should not differ much in the confirmation simulation, but at 30 s the values were significantly different, as may be seen in Table 2 (0.828 vs. 1.014). Because of the stochastic nature of the Monte Carlo simulations, the effect appears to be "washed out" after some time. In the original simulations, the values of α at 30 and 120 s were similar (0.984 vs. 1.027 and 0.852 vs. 0.848, respectively), and the values of α at 60 and 90 s were quite different (0.938 vs. 0.660 and 1.004 vs. 0.793, respectively). In general, the values of α computed from the confirmation simulation and the individual Monte Carlo simulation codes were not drastically different (with the exception of one simulation at 60 s, which we attributed to simulation noise).

It is possible to estimate the components of the variance in α for the confirmation procedure and the original Monte Carlo simulation codes. The variance can be regarded as having three independent components: the variance due to the random noise in the simulation codes; the variance due to the application of different potentials to the simulations coupled to the resistance code; and the variance due to the periodic boundary condition assumption.

The variance due to the random noise in the simulation codes can be estimated directly from the confirmation procedure simulation,

$$\sigma^2_{\text{random}} = \frac{1}{3}\sum_{i=1}^{4}(\alpha^a_{c_i} - \alpha^b_{c_i})^2, \tag{18}$$

where α^a_c is the spatial scaling exponent for the confirmation simulation associated with the electrical contact point and α^b_c is the spatial scaling exponent associated with the neighboring simulation.

The variance that is due to the application of different potentials to the Monte Carlo simulation codes that were coupled to the resistance code is

$$\sigma^2_{\text{random}} + 4\sigma^2_{\text{single potential}} = \frac{1}{3}\sum_{i=1}^{4}(\alpha^a_i - \alpha^b_i)^2, \tag{19}$$

where α^a is the spatial scaling exponent associated with the Monte Carlo simulation code at the electrical contact point and α^b is the spatial scaling exponent associated with the Monte Carlo simulation code next to the electrical contact point. The factor of 4 in Equation (19) takes into account the variance due to the different potentials in the Monte Carlo simulation codes.

The variance that is due to the periodic boundary condition assumption can then be estimated from

$$\sigma^2_{\text{random}} + \sigma^2_{\text{single potential}} + \sigma^2_{\text{BC}} = \frac{1}{3}\sum_{i=1}^{4}(\alpha_i^a - \alpha_{c_i}^a)^2 \qquad (20)$$

or

$$\sigma^2_{\text{random}} + \sigma^2_{\text{single potential}} + \sigma^2_{\text{BC}} = \frac{1}{3}\sum_{i=1}^{4}(\alpha_i^b - \alpha_{c_i}^b)^2. \qquad (21)$$

However, the two should produce slightly different results because the time variance in the potential is greater farther from the electrical contact point.

From the data given in Table 2, $\sigma^2_{\text{random}} = 0.018$, $\sigma^2_{\text{single potential}} = 0.006$, σ^2_{BC} computed from Equation (20) is 0.006, and σ^2_{BC} computed from Equation (21) is 0.003. Clearly, the largest variance in the system is due to the stochastic noise in the Monte Carlo simulation code, which is indicated by the fact that σ^2_{random} is three times larger than the next biggest variance. The other variances are relatively small by comparison. The fact that $\sigma^2_{\text{single potential}}$ is small indicates that our average potential assumption across the entire Monte Carlo domain in the confirmation simulation does not introduce large errors into the simulations. Furthermore, the values computed for σ^2_{BC} indicate that our methodology for linking the Monte Carlo simulation codes to the resistance code where the codes all have periodic boundary conditions does not introduce significant error into the scaling analysis results. Additionally, as predicted, the value of σ^2_{BC} computed from Equation (20) is greater than that computed from Equation (21).

The values of the temporal scaling exponent β at 120 s of deposition are shown in Table 3. The values of β for each side of the domain should not differ much in the confirmation simulation, just as the values of α should not differ. In the confirmation simulation, the values of β did not differ drastically and were similar to the values computed from the two Monte Carlo simulation codes.

The confirmation procedure gives some insight into the relative sources of uncertainty. It has been shown that assuming small Monte Carlo domains with a single applied potential and periodic boundary conditions introduces variations that are small compared with the fluctuations due to the stochastic noise in the Monte Carlo simulation codes. It is therefore concluded that the computational cost of using larger domains cannot be justified for the current study and that the approximations made by using small Monte Carlo domains each having a single applied potential and periodic boundary conditions do not drastically alter the physical accuracy of the simulations.

Conclusions

A method is developed for linking multiple simulation codes to create a multiscale simulation that includes continuum as well as stochastic phenomena. The method is demonstrated by application to the electrodeposition of copper on a resistive seed/barrier layer. The macroscale code considers the effect of radial potential distribution in the metal film on the electrochemical reaction rate distribution. The microscale code simulates local adsorption–reaction and surface diffusion events associated with deposition of 100-nm pseudoparticles from an additive-free solution onto an initially flat featureless copper surface. The situation is inherently multiscale in the sense that the macroscopic (continuum) potential distribution exerts a significant effect on the local microscopic (stochastic) roughness which, moreover, changes in time as the deposit grows thicker. Simulations were carried out for the arrangement shown in Figure 1, where the macroscale code was linked to ten Monte Carlo simulation codes.

Example simulations are carried out over a range of parameter space (Table 1) for both constant-potential (Figures 2 and 3) and constant-current (Figures 5 and 6) modes. The effect of dimensionless parameters on the uniformity of the reaction rate distribution at the onset is summarized (Figure 4). For both constant-potential and constant-current modes, it was found that the spatial scaling coefficients for roughness evolution [Figures 3(b) and 6(b)] were highest at the contact point to the film (and decreased toward the center) while the temporal scaling coefficients [Figures 3(c) and 6(c)] were lowest at the contact point (and increased toward the center).

By comparing a limited number of simulations that were identical except for the use of different random seed numbers for the Monte Carlo calculations, it was found that the maximum potential difference in the potential distribution was 8% of the applied potential, found near the center of the wafer; the maximum difference in deposit thickness was about 25%; the maximum difference in values of scaling exponents was found at the contact side and was 25% for the spatial exponent and 75% for the temporal exponent. The influence of the seed number on potential, current, and scaling results points to the need for making a sufficient number of duplicate simulations with random seed numbers in order to average out stochastic noise.

A confirmation procedure showed that fluctuations in the scaling analysis results that can be attributed to the

assumption of periodic boundary conditions are small in comparison with fluctuations in the scaling analysis results that are due to the stochastic noise in the Monte Carlo codes (Tables 2 and 3). That is, the computational approach which uses small Monte Carlo simulation domains with periodic boundary conditions provides an efficient method for multiscale calculations that does not significantly alter the physical accuracy of the simulations. It is therefore concluded that the computation framework presented here could provide yet more accurate results by averaging multiple duplicate simulations with use of multiple random seed numbers, as indicated in the previous paragraph.

Experimental measurements of roughness evolution can be used to test the validity of numerical simulations. Procedures were reported recently for estimating values of the most sensitive parameters for copper electrodeposition with a four-additive system [24]. The procedures used experimental data and a multiscale simulation code composed of a KMC code coupled to a continuum code.

There are a large number of applications for which multiscale continuum/stochastic systems could be investigated with the method outlined in this paper. More sophisticated codes could be used for the continuum portion, including continuum codes that predict the current and potential distribution in deposition tools, as well as stochastic codes that incorporate additional phenomena. Examples might include potential-dependent nucleation directly onto barrier layers, the influence of multiple solution additives on nucleation and roughness evolution, and shape evolution during electrodeposition in complex geometries such as rough surfaces and on-chip trenches and vias.

Acknowledgments

This work was supported by the National Science Foundation (CTS-0135621 and ACI 96-19019), and by an IBM Faculty Partnership Award. Any opinions, findings, and conclusions or recommendations expressed in this material are those of the authors and do not necessarily reflect the views of the National Science Foundation. Computer time was provided through the National Science Foundation Partnership for Advanced Computing Infrastructure via the National Computational Science Alliance (NCSA, University of Illinois). During the period of this study, T.O.D. was awarded the H. G. Drickamer Fellowship by the Department of Chemical and Biomolecular Engineering of the University of Illinois.

**Trademark or registered trademark of Silicon Graphics, Inc. or MIPS Technologies, Inc.

Appendix 1: List of symbols

- A Height of the deposit; [dimensionless]
- c_b Reactant concentration in the bulk solution; [g-mole/cm^3]
- c_s Reactant concentration at the electrode surface; [g-mole/cm^3]
- C_s Reactant concentration at the electrode surface; [dimensionless]
- D_b Bulk diffusion coefficient; [nm^2/s]
- D_s Surface diffusion coefficient; [nm^2/s]
- E Energy (barrier); [J/molecule]
- F Faraday's constant; [C/equivalent]
- h Root-mean-squared height; [cm]
- H Height of deposit; [cm]
- $H^\bullet$ Height of the deposit at the electrical contact point; [cm]
- H_0 Initial height of the deposit; [cm]
- i Current density in the electrode; [A/cm^2]
- $i^\bullet$ Current density in the electrode at the electrical contact point; [A/cm^2]
- i_0 Exchange current density of the electrode reaction at bulk concentrations; [A/cm^2]
- I Current; [A]
- j Local reaction rate (current density) along the electrode surface; [A/cm^2]
- J Local reaction rate (current density) along the electrode surface; [dimensionless]
- k Mass transfer coefficient; [cm/s]
- k_{rxn} Reaction rate constant; [nm/s]
- L Length across surface; [cm]
- M Molecular weight; [g/mole]
- n Number of charge equivalents; [equivalents]
- r Radial position on the wafer; [cm]
- R Ideal gas constant; [J/(mole*K)]
- R_0 Radius of the wafer; [cm]
- R_a Radial position; [dimensionless]
- t Time; [s]
- T Temperature; [K]

Appendix 2: List of Greek symbols

- α Spatial scaling exponent; [dimensionless]
- α_T Tafel slope; [dimensionless]
- β_{CD} Current density in the electrode at the electrical contact point; [dimensionless]
- β Temporal scaling exponent; [dimensionless]
- Γ Ratio of ohmic resistance to mass-transfer resistance; [dimensionless]
- ϕ_m Potential in the electrode; [V]
- $\phi_m^\bullet$ Potential in the electrode at the electrical contact end; [V]
- ϕ_m^e Potential in the electrode at equilibrium; [V]
- $\phi_s^\bullet$ Potential in the solution at the electrical contact end of the cell; [V]

ϕ_s^e Potential in the solution at equilibrium; [V]
ϕ_s^s Potential in the solution at the electrode surface; [V]
Φ_a Applied potential; [dimensionless]
Φ_m Potential in the electrode; [dimensionless]
η Overpotential; [V]
η_c Concentration overpotential in the solution; [V]
η_s Charge-transfer overpotential at the electrode–solution interface; [V]
η_Ω Ohmic overpotential in the electrode; [V]
ρ_{Cu} Density of copper; [g/cm^3]
σ Conductivity of metal electrode; [Ω^{-1}-cm^{-1}]
σ^2_{BC} Variance in α due to periodic boundary conditions; [dimensionless]
σ^2_{random} Variance in α due to the simulation noise; [dimensionless]
$\sigma^2_{single\ potential}$ Variance in α due to single applied potential; [dimensionless]
τ Time; [dimensionless]
ξ Ratio of ohmic resistance to charge-transfer resistance; [dimensionless]
Ξ Ratio of ohmic resistance to charge-transfer resistance; [dimensionless]

References

1. R. Liu, C. Pai, and E. Martinez, "Interconnect Technology Trend for Microelectronics," *Solid-State Electron.* **43,** 1003–1009 (1999).
2. E. K. Broadbent, E. J. McInerney, L. A. Gochberg, and R. L. Jackson, "Experimental and Analytical Study of Seed Layer Resistance for Copper Damascene Electroplating," *J. Vac. Sci. Technol. B* **17,** 2584–2595 (1999).
3. P. R. Westmoreland, P. A. Kollman, A. M. Chaka, P. T. Cummings, K. Morokuma, M. Neurock, E. B. Stechel, and P. Vashishta, *WTEC Panel Report on Applications of Molecular and Materials Modeling,* International Technology Research Institute World Technology (WTEC) Division, Baltimore, 2002.
4. U. Landau, J. D'Urso, A. Lipin, Y. Dordi, A. Malik, M. Chen, and P. Hey, "A Novel Electrolyte Composition for Copper Plating in Wafer Metallization," *Extended Abstracts of the 195th Meeting of the Electrochemical Society*, **PV 99-9,** Abstract No. 263, 25–40 (1999).
5. K. Takahashi, "Electroplating Copper onto Resistive Barrier Films," *J. Electrochem. Soc.* **147,** 1414–1417 (2000).
6. C. Tobias and R. Wijsman, "Theory of the Effect of Electrode Resistance on Current Density Distribution in Electrolytic Cells," *J. Electrochem. Soc.* **100,** 459–467 (1953).
7. R. Alkire, "Transient Behavior During Electrodeposition into a Metal Strip of High Ohmic Resistance," *J. Electrochem. Soc.* **118,** 1935–1941 (1971).
8. M. Matlosz, P. H. Vallotton, A. C. West, and D. Landolt, "Nonuniform Current Distribution and Thickness During Electrodeposition onto Resistive Substrates," *J. Electrochem. Soc.* **139,** 752–761 (1992).
9. O. Lanzi and U. Landau, "Terminal Effect at a Resistive Electrode Under Tafel Kinetics," *J. Electrochem. Soc.* **137,** 1139–1143 (1990).
10. H. Kawamoto, "Numerical-Calculation of Secondary Current Distribution in a 2-Dimensional Electrochemical-Cell with a Resistive Electrode," *J. Appl. Electrochem.* **22,** 1113–1116 (1992).
11. H. Deligianni, J. O. Dukovic, E. G. Walton, R. J. Contolini, J. Reid, and E. Patton, "Model of Wafer Thickness Uniformity in an Electroplating Tool," *Extended Abstracts of the 195th Meeting of the Electrochemical Society*, **PV 99-9,** Abstract No. 270, 83–95 (1999).
12. W. H. Press, S. A. Teukolsky, W. T. Vetterling, and B. P. Flannery, *Numerical Recipes in Fortran: The Art of Scientific Computing,* Second Edition, Cambridge University Press, Cambridge, England, 1992.
13. T. J. Pricer, M. J. Kushner, and R. C. Alkire, "Monte Carlo Simulation of the Electrodeposition of Copper, I: Additive-Free Acidic Sulfate Solution," *J. Electrochem. Soc.* **149,** C396–C405 (2002).
14. T. O. Drews, E. G. Webb, D. L. Ma, J. Alameda, R. D. Braatz, and R. C. Alkire, "Coupled Mesoscale-Continuum Simulations of Copper Electrodeposition in a Trench," *AIChE J.* **50,** 226–240 (2004).
15. T. O. Drews, J. C. Ganley, and R. C. Alkire, "Evolution of Surface Roughness During Copper Electrodeposition in the Presence of Additives: Comparison of Experiments and Monte Carlo Simulations," *J. Electrochem. Soc.* **150,** C325–C334 (2003).
16. D. Maroudas, "Multiscale Modeling of Hard Materials: Challenges and Opportunities for Chemical Engineering," *AIChE J.* **46,** 878–882 (2000).
17. J. Lu and M. J. Kushner, "Trench Filling by Ionized Metal Physical Vapor Deposition," *J. Vac. Sci. Technol. A* **19,** 2652–2663 (2001).
18. G. A. Bird, *Molecular Gas Dynamics and the Direct Simulation of Gas Flows,* Clarendon Press, Oxford, England, 1994.
19. C. K. Birdsall and A. B. Langdon, *Plasma Physics via Computer Simulation,* McGraw-Hill Book Co., Inc., New York, 1985.
20. M. A. Katsoulakis, A. J. Majda, and D. G. Vlachos, "Coarse-Grained Stochastic Processes for Microscopic Lattice Systems," *Proc. Natl. Acad. Sci. USA* **100,** 782–787 (2003).
21. T. O. Drews, R. D. Braatz, and R. C. Alkire, "Multiscale Coarse-Grained Kinetic Monte Carlo Simulations of Copper Electrodeposition with Additives," *Int. J. Multiscale Computational Eng.* **2,** 313–327 (2004).
22. T. O. Drews, A. Radisic, J. Erlebacher, R. D. Braatz, P. C. Searson, and R. C. Alkire, "Atomic-Scale Kinetic Monte Carlo Simulations of Copper Nucleation: Investigation of Attachment Limited Rate Laws," *Extended Abstracts of the 204th Meeting of the Electrochemical Society,* Abstract No. 699 (2003).
23. W. M. Tong and R. S. Williams, "Kinetics of Surface Growth—Phenomenology, Scaling, and Mechanisms of Smoothening and Roughening," *Annu. Rev. Phys. Chem.* **45,** 401–438 (1994).
24. T. O. Drews, F. Xue, X. Li, H. Deligianni, P. M. Vereecken, E. I. Cooper, P. C. Andricacos, R. D. Braatz, and R. C. Alkire, "Parameter Estimation of a Copper Electrodeposition Additive Mechanism Using Data Obtained from a D-Optimal Experimental Design," *Extended Abstracts of the 204th Meeting of the Electrochemical Society,* Abstract No. 698 (2003).

Received January 28, 2004; accepted for publication May 18, 2004; Internet publication December 7, 2004

Timothy O. Drews *University of Illinois, Department of Chemical and Biomolecular Engineering, 600 S. Mathews Avenue, Urbana, Illinois 61801 (todrews@uiuc.edu).* Dr. Drews received a B.S. degree in chemical engineering and engineering and public policy from Carnegie Mellon University in 1999. He completed an M.S. degree in 2001 and a Ph.D. degree in 2004, both in chemical engineering, from the University of Illinois at Urbana–Champaign. His research has focused on the creation and analysis of a Kinetic Monte Carlo (KMC) simulation code for electrodeposition. His Ph.D. work addressed a key weakness in simulating copper electrodeposition: the modeling of nucleation on the surface of the wafer. Additionally, he has created a multiscale simulation code for copper electrodeposition into trenches that dynamically couples continuum and discrete (KMC) codes, which is an advance in that both of these codes run continuously as dynamic codes. Dr. Drews is the 2004 Ross J. Martin Award winner for outstanding research achievement by a graduate student from the College of Engineering at the University of Illinois.

Sriram Krishnan *Indiana University, Department of Computer Science, 150 S. Woodlawn Avenue, Bloomington, Indiana 47405 (srikrish@cs.indiana.edu).* Mr. Krishnan received a B.E. degree in computer engineering from the University of Mumbai, India, in 1999, and an M.S. degree in computer science from Indiana University in 2001; he expects to receive a Ph.D. degree in computer science from Indiana University in 2004. His research has been on software components for grid computing. Specifically, he has designed and implemented XCAT3, a component framework conforming to the Common Component Architecture (CCA) that enables orchestration of complex distributed applications on the Grid. In addition, he has developed a user-level distributed checkpointing mechanism for fault tolerance of such components, and for migration of individual components in order to respond to dynamic grid environments. Mr. Krishnan has also worked at Argonne National Laboratories designing and implementing workflow technologies for grid services, and at the IBM Thomas J. Watson Research Center, investigating desktop grids for scientific and business applications.

Jay C. Alameda, Jr. *University of Illinois, National Center for Supercomputing Applications, 605 E. Springfield Avenue, Champaign, Illinois 61820 (jalameda@ncsa.uiuc.edu).* Mr. Alameda received a B.S. degree in chemical engineering from the University of Notre Dame in 1986 and an M.S. degree in nuclear engineering from the University of Illinois at Urbana–Champaign in 1991. Since 1990 he has been a research programmer at the National Center for Supercomputing Applications (NCSA), where he currently leads the NCSA effort in grid computing, with emphasis on applications in environmental hydrology and chemical engineering.

Dennis Gannon *Indiana University, Department of Computer Science, 150 S. Woodlawn Avenue, Bloomington, Indiana 47405 (gannon@cs.indiana.edu).* Dr. Gannon is a professor in the Department of Computer Science at Indiana University, and he is its current chair. His previous positions include those of assistant and associate professor in the Department of Computer Science at Purdue University. From 1985 to 1990, he was also a senior visiting research scientist at the Center for Supercomputer Research and Development, University of Illinois, where he worked on the Cedar multiprocessor project. His current work is on the design of software component architectures for distributed scientific applications, and on the study of the architecture of grid systems. From 1995 to the present he has been a member and one of the co-founders of the Common Component Architecture (CCA) project. From 1998 to 2000, he worked at NASA Ames Research Center on the Information Power Grid project, and he was a founding participant in the Global Grid Forum (where he now co-chairs the Grid Computing Environments Research Group and the Open Grid Service Architecture working group). Dr. Gannon is also the Science Director for the new Indiana Pervasive Technologies Laboratories. Since 2000, he has also served as the Chief Computer Scientist for the NCSA Alliance.

Richard D. Braatz *University of Illinois, Department of Chemical and Biomolecular Engineering, 600 S. Mathews Avenue, Urbana, Illinois 61801 (braatz@uiuc.edu).* Dr. Braatz received a B.S. degree from Oregon State University (1988) and M.S. and Ph.D. degrees from the California Institute of Technology (1991, 1993, respectively). After a postdoctoral year at DuPont, in 1994 he joined the faculty of chemical engineering at the University of Illinois, where he is now Professor and University Scholar. His interests are currently in multiscale systems theory and its applications to semiconductor processes, nanotechnology, and biotechnology. He has co-authored three books and more than 80 journal papers. His research awards include the Xerox Award for Faculty Research (1999), the Donald P. Eckman Award of the American Automatic Control Council (2000), and the CAST Directors' Award of the American Institute of Chemical Engineers (2003).

Richard C. Alkire *University of Illinois, Department of Chemical and Biomolecular Engineering, 600 S. Mathews Avenue, Urbana, Illinois 61801 (r-alkire@uiuc.edu).* Dr. Alkire received a B.S. degree from Lafayette College in 1963, and M.S. and Ph.D. degrees from the University of California at Berkeley in 1965 and 1968, all in chemical engineering. Since 1969 he has been on the faculty at the University of Illinois, where he now holds the Charles J. and Dorothy G. Prizer endowed chair in chemical engineering. He served as Head of Chemical Engineering from 1986 to 1994 and Vice Chancellor for Research and Dean of the Graduate College from 1994 to 1999. His research interests are in electrochemical engineering, especially in the use of high-performance computing to integrate experimental data with multiscale simulations. A member of the National Academy of Engineering since 1988, he recently received the 2004 Vittorio de Nora Award and Gold Medal of The Electrochemical Society.

Copyright of IBM Journal of Research & Development is the property of IBM Corporation/IBM Journals and its content may not be copied or emailed to multiple sites or posted to a listserv without the copyright holder's express written permission. However, users may print, download, or email articles for individual use.